HCHO Sensing Mechanism of In4Sn3O12 Revealed by DRIFTS and DFT

Tingqiang Yang, Anne Hémeryck, Suman Pokhrel, Wen Chen, Lutz Mädler, Udo Weimar, Nicolae Barsan

HCHO Sensing Mechanism of $In_4Sn_3O_{12}$ Revealed by DRIFTS and DFT

Tingqiang Yang,[1,2] Anne Hemeryck,[2,*] Suman Pokhrel,[3] Wen Chen,[4] Lutz Mädler,[3] Udo Weimar,[1] Nicolae Barsan[1,*]

[1] Institute of Physical and Theoretical Chemistry and Center for Light-Matter Interaction, Sensors & Analytics (LISA+), University of Tübingen, 72076 Tübingen, Germany

[2] LAAS-CNRS, Université de Toulouse, CNRS, 31400 Toulouse, France

[3] Foundation Institute of Materials Science (IWT), Department of Production Engineering, University of Bremen, 28359 Bremen, Germany

[4] State Key Laboratory of Silicate Materials for Architectures, School of Materials Science and Engineering, Wuhan University of Technology, 430070 Wuhan, China

*Corresponding authors:

Nicolae Barsan: nb@ipc.uni-tuebingen.de

Anne Hemeryck: anne.hemeryck@laas.fr

Abstract

The combination of operando DRIFTS measurement and DFT calculation reveals the counterintuitive HCHO sensing mechanism of $In_4Sn_3O_{12}$. It is merely partial oxidation of HCHO into formate (or HCOOH) with medium activation energy (0.43−0.68 eV) and sufficient electron donation effect that is responsible for the sensor signal at the optimum temperature of 200 ℃. The Sn (3a)-connected O is the active site and plays key roles in both HCHO adsorption and partial oxidation.

1. Introduction

Formaldehyde (HCHO), a harmful indoor air pollutant normally emitted from building materials and some household furniture, can not only irritate the eyes and respiratory tract but also cause pneumonia and even cancer.[1-3] Distributed HCHO monitoring is very necessary and requires high-performance sensors with low cost and low power consumption. Gas sensors based on semiconducting metal oxides (SMOX), which are not only low-cost and energy-saving but also have been commercially utilized, could be a solution, if sufficiently selective.[4-7]

$In_4Sn_3O_{12}$ nanoparticles with good selectivity to HCHO against CO, ethanol, benzene and toluene have been proposed in our previous research, and the sensor signal to HCHO is also ultrahigh.[8-9] Additionally, the synthesis by flame spray pyrolysis (FSP) renders mass production and thus low cost. The surprising performance makes the $In_4Sn_3O_{12}$ a promising material for sensing HCHO, while this surprise has always been accompanied by the puzzle of the underlying mechanism.

In the gas sensing mechanism of SMOX sensors, surface oxygen species play the key role.[5-7, 10-15] Taking n-type SMOX as the example, when the sensors operate in air and at temperatures between 200 and 400 °C, oxygen molecules are adsorbed and ionized by capturing electrons from the conduction band, by that, localizing then at the SMOX surface. The result is the formation of electron-depletion layer, which increases the resistance of the sensing layer.[10] In the presence of reducing gases, the ionosorbed and reactive oxygen species can be consumed, which makes it possible for the electrons to return to the conduction band by that decreasing the surface charge and the sensing layer resistance. Besides the adsorbed oxygen, in some SMOX, surface lattice oxygen also participates in the sensing reaction.[16] In that case, the reducing gas reacts with the surface lattice oxygen and generates oxygen vacancies (V_O). When the reducing gases are no more present, the V_O can be refilled by oxygen molecule or oxygen atom if the molecule dissociates. For the case of HCHO sensing mechanism of $In_4Sn_3O_{12}$, the first question is whether the ionosorbed oxygen or the lattice oxygen is the reaction partner/active oxygen species.

The second question is about the final product of HCHO after the reaction with surface oxygen species. The volatile organic compounds (VOCs) molecules are extensively considered to be completely combusted to CO_2 and H_2O during gas sensing process.[17-20] This makes difficult to explain the good selectivity to HCHO against other VOCs which actually consumes more oxygen species if completely oxidized.

To reveal the HCHO sensing mechanism of $In_4Sn_3O_{12}$ is not only a very interesting scientific question but, but also have a practical relevance because it could open new avenues for SMOX gas sensors. Encouraged by the success of the combination between in operando Diffuse Reflectance Infrared Fourier Transform Spectroscopy (DRIFTS) with Density Functional Theory (DFT) calculations,[21] we have applied the same approach to reveal HCHO sensing mechanism of $In_4Sn_3O_{12}$. Experimentally, N_2/O_2, H_2O/D_2O as well as HCHO DRIFTS are measured to reveal adsorption and reaction behaviors of O_2, H_2O and especially HCHO at $In_4Sn_3O_{12}$ surface. Theoretically, by DFT, the HCHO adsorptions and reactions are simulated at different $In_4Sn_3O_{12}$ (001) surfaces: 1) stoichiometric surface, 2) surface with an oxygen vacancy (V_O) filled by an O_2 molecule ($In_4Sn_3O_{12}$ (001)_O_2/V_O), and 3) surface with a terminal hydroxyl group ($In_4Sn_3O_{12}$ (001)_OH_t).

2. Experimental and computational details

2.1 Details of DRIFTS measurement

The $In_4Sn_3O_{12}$ nanoparticles in this research were synthesized by the same FSP method as in our previous research.[8-9] X-ray diffraction (XRD) was measured and the Rietveld refinement demonstrated the $In_4Sn_3O_{12}$ nanoparticles in around 4.7 nm, which is consistent with scanning electron microscope (SEM) in image (Figure S1). The sensor devices were fabricated by screen printing to make the sensor layer denser and thus make DRIFTS more evident. In our previous research, we explored the temperature range between 250 and 350 °C and found the highest sensor signal to HCHO at 250 °C.[9] Additional measurements conducted from 100 to 300 °C, revealed that the optimum temperature is around 150−200 °C, as shown in Figure S2. Because of better stability and faster response/recovery times we chose 200 °C.

Not only HCHO DRIFTS was measured to explore HCHO reaction at $In_4Sn_3O_{12}$ (001) surface, but also N_2-O_2 and H_2O-D_2O exchange DRIFTS were measured in advance to explore O_2 and water adsorption behavior at the surface. The sensor devices for HCHO sensing measurement and DRIFTS were fabricated at the same time. The device for DRIFTS had not been used for any gas sensing measurement before. During DRIFTS measurement, the device was heated to 200 °C by an external power supply (Agilent E3630A), and the response of the gas sensors was recorded using a digital multimeter (Keithley 199 or Keithley 2000). Before each measurement, all sensors were maintained at the given operation temperature until a stable baseline is reached. DRIFTS measurement was done using a commercial six-mirror optic

(Harrick Praying Mantis) and a homemade gas sensor cell with a KBr window. All spectra were recorded on an FT-IR spectrometer (Bruker Vertex 80V) with an MCT mid-band detector and an external high performance Globar. Each single channel (SC) spectrum is an average of 1024 scans over 15 minutes and was measured with a spectral resolution of 1 cm^{-1}. Eight SC spectra were obtained during two-hour exposure of the device to each atmosphere. A N_2/O_2 DRIFTS example is shown in Figure S3. An absorbance (A) spectrum can be calculated by **Eq. 1** with selecting one spectrum as reference and the other as comparison.

$$A = -log\left(\frac{SC_{Comparison}}{SC_{Reference}}\right) \quad \text{Eq. 1}$$

2.2 Computational details

Spin-unrestricted DFT calculation was performed with a periodic $In_4Sn_3O_{12}$ (001) surface supercell by Dmol3 package.[22-23] General gradient approximation (GGA) in the form of a Perdew–Burke–Ernzerhof (PBE) was selected for the exchange–correlation functional, and a DFT-D correction was executed to take van der Waals interaction into consideration. Inner electrons of atoms are treated by using DFT Semi-core Pseudopots.[24] A 3 × 3× 3 or 2 × 2 × 1 Monkhorst–Pack grid was respectively used for Brillouin-zone integration of the primitive cell or the surface supercell. For geometry optimization, convergence tolerance is 2×10^{-5} hartree in energy, 4×10^{-3} hartree $Å^{-1}$ in force, and 5×10^{-3} Å in displacement. For transition state (TS) search, a linear synchronous transit/quadratic synchronous transit (LST/QST) method was used with root-mean-square convergence of 0.002 hartree $Å^{-1}$. To analyze the charge transfer effect, Mulliken charge was calculated.

The adsorption energy (E_{ads}), formation energy of V_O ($E[V_O]$), activation energy (E_a) and reaction energy (E_{react}) are defined as

$$E_{ads} = E_{In4Sn3O12\ (001)\ +\ molecule} - E_{In4Sn3O12\ (001)} - E_{molecule} \quad \text{Eq. 2a}$$

$$E[V_O] = E_{In4Sn3O12\ (001)\_VO} + 1/2\ E_{O2} - E_{In4Sn3O12\ (001)} \quad \text{Eq. 2b}$$

$$E_a = E_{TS} - E_{reactant} \quad \text{Eq. 2c}$$

$$E_{react} = E_{procuct} - E_{reactant} \quad \text{Eq. 2d}$$

In Eq. 2a, $E_{In4Sn3O12\ (001)\ +\ molecule}$, $E_{In4Sn3O12\ (001)}$ and $E_{molecule}$ represent total energy of $In_4Sn_3O_{12}$ (001) adsorbed with gas molecule, total energy of $In_4Sn_3O_{12}$ (001) and that of a specific gas molecule. Similarly,

in Eq. 2b, $E_{In4Sn3O12\,(001)\_VO}$ and E_{O2} represent total energy of $In_4Sn_3O_{12}$ (001) with one V_O and that of one oxygen molecule. In Eq. 2c, d, $E_{reactant,}$ E_{TS} and $E_{procuct}$ mean energy at the beginning, transition state and end of a reaction.

2.3 Building and optimization of $In_4Sn_3O_{12}$ primitive cell

According to previous XRD and Rietveld analysis as well as transmission electron microscopic (TEM) analysis, $In_4Sn_3O_{12}$ is rhombohedral.[8-9] The structure is easily viewed in a hexagonal basis, with lattice parameters a = 9.46 Å and c = 8.86 Å.[25] One hexagonal $In_4Sn_3O_{12}$ primitive cell possesses 12 In, 9 Sn and 36 O atoms. For the metal atoms, there are two nonequivalent sites: the six-coordinated 3a position (1/7) and the seven-coordinated 18f position (6/7). The 3a positions are exclusively occupied by the Sn, while the 18f positions are randomly occupied by both Sn (2/7) and In (4/7).[26] The random occupation at the 18f position of Sn or In renders many (C_{18}^{6}) possible primitive cells. Actually, the primitive cell is composed of three M-O-M (M means metal) layers along [001] direction, and each layer has 7 metal atoms, as shown in Figure 1a−c. Supposing Sn atoms evenly distribute in each layer, there are not that many possibilities. Additionally, in the layer, the 3a position is surrounded by six 18f positions (Figure 1d). Finally, we have built a primitive cell, as shown in Figure 1e, making the three Sn atoms (one at 3a and the other two at 18f) in different shapes. By comparing with five other possible cells, we found that the primitive cell in Figure 1e is the most energetically favorable.

The Sn distribution in ecah layer makes the $In_4Sn_3O_{12}$ primitive cell lose the symmetry, while the cell is still quasi-hexagonal. The geometry optimized $In_4Sn_3O_{12}$ primitive cell is with parameters a = 9.698 Å, b = 9.694 Å, c = 8.978 Å, α = 89.287°, β = 90.197°, and γ = 120.340°, close to the experimental results.[8-9]

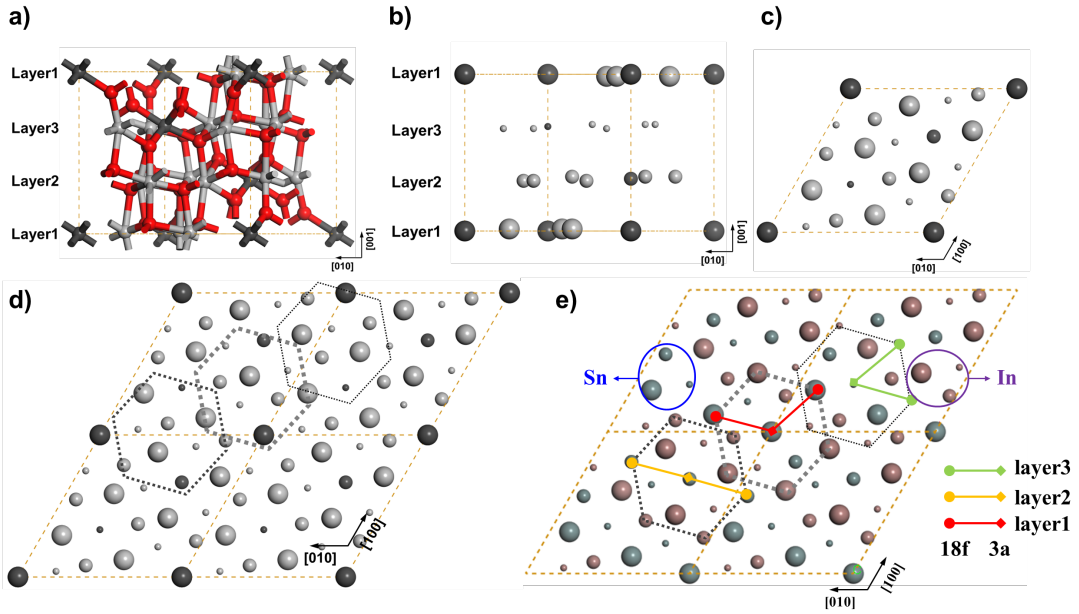

Figure 1 (a) The hexagonal $In_4Sn_3O_{12}$ primitive cell (3a position is in dark, 18f is in silver, and the red is oxygen atom), (b, c) the primitive cell with oxygen invisible showing three layers of metal atoms set in different radii, (d) the (2 × 2 × 1) primitive cell showing the arrangement of 3a and 18f metal atoms in each layer, and (e) the built and the most energetically favorable primitive cell.

2.4 Surface cleaving and optimization

With the optimized primitive cell, as shown in Figure S4a, $In_4Sn_3O_{12}$ (001) surface can be cleaved. The (001) plane can be mainly exposed because of the layer structure. Additionally, it has been previously characterized by TEM.[8] As is discussed in the part of building primitive cell, there are three different layers. If considering the cleaved surface normal to [001] and [00−1] directions, six possible surfaces can be obtained. After optimization and energy comparison, the most stable configuration of $In_4Sn_3O_{12}$ (001) surface is shown in Figure S4b, c. It is a (2 × 2) supercell with a 20 Å vacuum layer. The atoms of bottom layer are fixed to simulate bulk atoms, while the others can relax to simulate surface.

3. Results and discussion

3.1 DRIFTS

The $In_4Sn_3O_{12}$ shows remarkable resistance decline to 1.5 ppm and 10 ppm HCHO during DRIFTS measurement (Figure 2a). By referencing the stabilized response and recovery SC spectra to the last SC spectrum in initial air atmosphere (Figure 2a), one can clearly see the signals of various surface species in

the four overall DRIFTS absorbance spectra (Figure 2b). The dominant reaction product is the formate specie (Figure 2b), whose asymmetric vibration frequency ($\nu_{as}COO^-$) is positioned around 1576 cm^{-1} and symmetric vibration frequency (ν_sCOO^-) splits at 1381 and 1354 cm^{-1} due to interaction with CH.[27-30] In Figure 2b, additionally, two weak peaks at 2968 and 2887 cm^{-1} can be identified, which are attributed to $\nu_{as}CH_2$ and ν_sCH_2 of the adsorbed HCHO (or νCH of the generated formate).[27-30] The peaks are clearer and their intensity gradually increases in Figure 2c where the eight SC spectra obtained under 1 ppm HCHO exposure are referenced to the last SC spectrum acquired under the initial synthetic air exposure. Under exposure to 10 ppm HCHO, a weak peak of νC=O at 1788 cm^{-1} is observed in Figure 2g which is obtained when the eight SC spectra obtained in the presence of 10 ppm HCHO are referenced to the last SC spectrum acquired under the synthetic air exposure; it is determined by the molecularly adsorbed HCHO.[27] Most of the generated formate is desorbed after two hours re-exposure to air with the evident decreases of the peaks of $\nu_{as}COO^-$ and ν_sCOO^-, as shown in Figure 2f where eight eight SC spectra obtained under the second air exposure are referenced to the last SC spectrum acquired under 1.5 ppm HCHO. There are still some remaining formate species at the surface albeit one has to significantly zoom in to observe them (Figure 2b, lower panel).

Table 1 Observed signals of surface species in HCHO DRIFTS as well as their reported wavenumbers

Surface specie	Vibration mode	Vibration frequency in this work	The value in references
OH_t	νOH_t	3647−3654 cm^{-1}	3627−3720 cm^{-1} [31]
CH_2	$\nu_{as}CH_2$	2968−2970 cm^{-1}	2950−2970 cm^{-1} [27, 30]
	ν_sCH_2	2887−2889 cm^{-1}	2840−2870 cm^{-1} [27]
CH	ν_sCH	2887−2889 cm^{-1}	2840−2870 cm^{-1} [27-29]
OD_t	νOD_t	2690−2696 cm^{-1}	2577−2745 cm^{-1} [31]
C=O (HCHO)	νC=O	1788 cm^{-1}	1746 cm^{-1} [27]
COO^-	$\nu_{as}COO^-$	1571−1585 cm^{-1}	1550−1600 cm^{-1} [27-30]
	ν_sCOO^-	Spilt at 1381 and 1354 cm^{-1}	Split in 1410–1350 cm^{-1} [27]
$O_{2\ ads}$	$\nu O_{2\ ads}$	1132−1134 cm^{-1}	1060−1140 cm^{-1} [27] 1103, 1137 cm^{-1} [32]
In-O, Sn-O	νInO, νSnO	~1000 cm^{-1}	~1000 cm^{-1} (νM-O) [27]

Surface oxygen species (lattice oxygen or adsorbed oxygen) are influenced by the HCHO exposure: A pronounced valley centering around 1000 cm^{-1} corresponds to the vibration of M-O bond (νInO and νSnO) (Figure 2b, d, g); [21, 27] during recovery and under exposure to oxygen in a N_2 background is an opposite broad hill observed (Figure 2f, Figure S3). Inside the spectral region, there is a distinctive feature – a small but sharp peak at 1134 cm^{-1} – that can be attributed to vibration of the molecular oxygen ion O_2^- ($\nu O_{2\ ads}$).[27, 32] To our knowledge, it is the first experimental observation of that specie, and its involvement in gas sensing, obtained in operando conditions. A reported observation is at the surface of CeO_2 catalyst with in situ Raman spectroscopy, but at temperatures below 120 °C.[32]

Also, the density of surface terminal hydroxyl group (OH_t) varies under HCHO exposure. Clear decrease and increase of νOH_t around 3654 cm^{-1},[28-31, 33] identified by H_2O-D_2O exchange DRIFTS (Figure S5), are observed when $In_4Sn_3O_{12}$ is exposed to HCHO and re-exposed to air (Figure 1b, c ,e). Because the H_2O-D_2O exchange DRIFTS is performed beforehand, some OD_t groups are still present at the surface during the HCHO exposure measurement. Hence, a decrease at 2690 cm^{-1} (νOD_t) is observed in Figure 2b, c. Despite of the absence of D_2O during the recovery process following the 1.5-ppm-HCHO exposure, a small peak at 2696 cm^{-1} (νOD_t) still emerges in Figure 2e which is obtained by referring the eight SC spectra in second-round air to the last SC spectrum in 1.5 ppm HCHO. The reappearance of 2696 cm^{-1} (νOD_t) implies that some D atoms of OD_t might not desorbed but merely migrate to another site and it could return to OD_t after re-exposure to air.

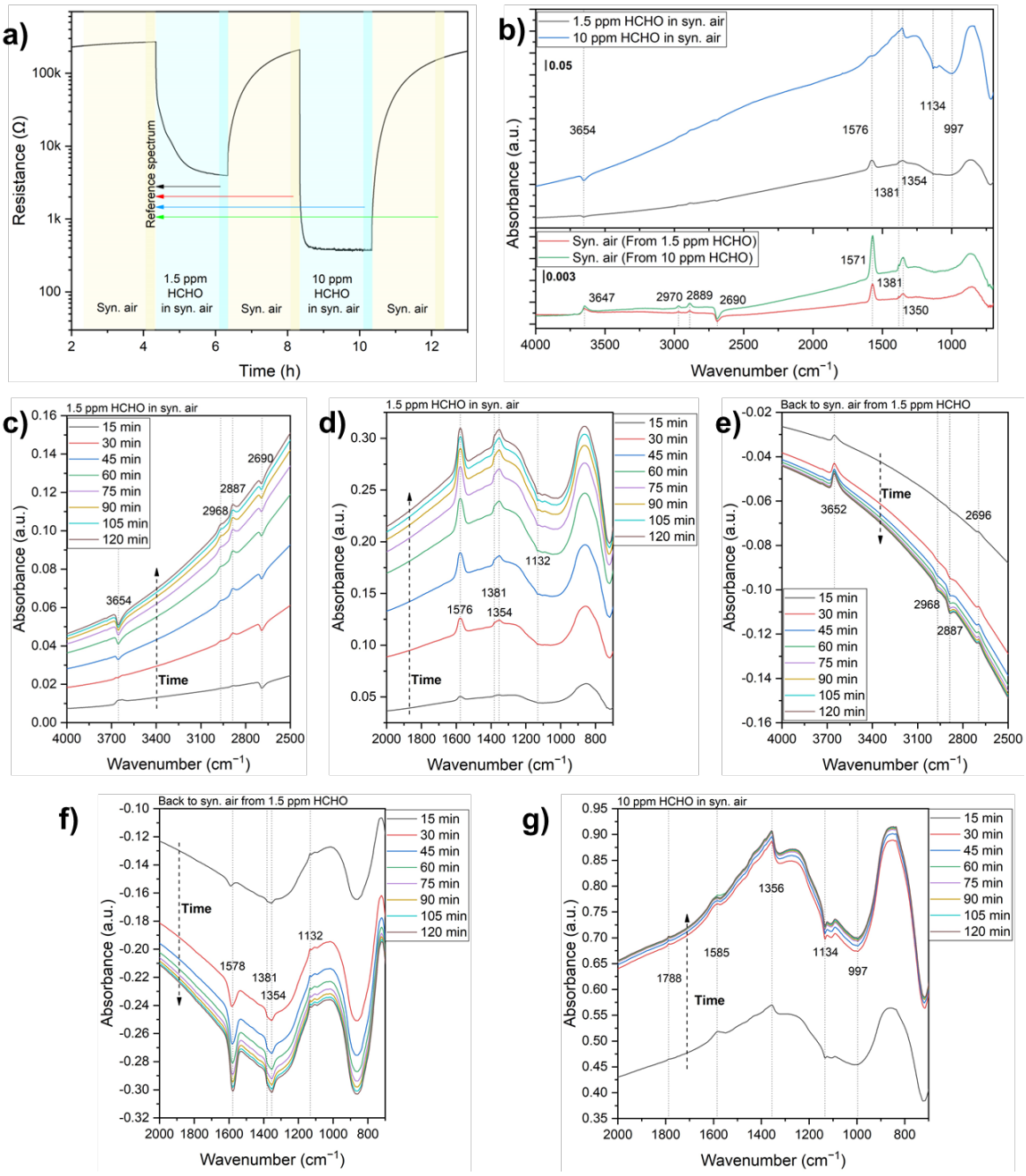

Figure 2 DRIFTS results measured at 200 °C. (a) Resistance curve of the sensor device during HCHO DRIFTS measurement, (b) absorbance spectra by referencing the last single channel (SC) spectra under the 1.5 ppm HCHO exposure, the second air exposure, the 10 ppm HCHO exposure and the third air exposure to the last SC spectrum under first air exposure, (c, d) eight absorbance spectra during 2 h 1.5 ppm HCHO exposure referrenced to the last SC spectrum in the first air exposure, (e, f) eight absorbance spectra during second air exposure referenced to the last SC spectrum under 1.5 ppm HCHO exposure, and (g) eight absorbance spectra during 2 h 10 ppm HCHO exposure referenced to the last spectrum in the second air exposure.

The DRIFTS suggests that HCHO is partially oxidized into formate species (or HCOOH) and that no combustion to CO_2 or CO takes place:

- The presence of -CH_2- (2968 and 2887 cm^{-1}) and the absence (or very little in 10 ppm HCHO) of C=O (1788 cm^{-1}) demonstrates the generation of dioxymethylene;[27-30, 34-35]
- The generated dioxymethylene is then oxidized into formate;
- Finally, the formate specie desorbs as HCOOH without being further oxidized (Eq. 3, in which the asterisk indicates an adsorbed species);
- Oxygen specie and OH_t take part in the processes, and the active O in Eq. 3a could be the O of OH_t.

$$HCHO+O\rightarrow *OCH_2O \quad \text{Eq. 3a}$$

$$*OCH_2O\rightarrow *HCOO+*H \quad \text{Eq. 3b}$$

$$*HCOO+*H\rightarrow HCOOH \quad \text{Eq. 3c}$$

The counterintuitive partial oxidation of HCHO arouses several questions: What is the exact role of oxygen species and OH_t? What are the reaction route and corresponding energy profile? How does it result in huge changes in resistance, by Eq. 3a or Eq. 3b?

3.2 DFT

To answer the questions, we resort to DFT simulation with the focus on oxygen species and OH_t involving surfaces of stoichiometric $In_4Sn_3O_{12}$ (001), $In_4Sn_3O_{12}$ (001)_O_2/V_O and $In_4Sn_3O_{12}$ (001)_OH_t.

The examination of various, possible HCHO adsorption sites and the V_O formation energy identify the Sn (3a)-connected O as the active site (Figure S6−8). The, called in the following, active O plays significant roles in both HCHO adsorption and partial oxidation (Figure 3a). The adsorption takes place with the active O catching the C and the surface Sn (18f) bonding to the O (HCHO), making the HCHO spontaneously transform into dioxymethylene with an adsorption energy (E_{ads}) of −1.87 eV (Figure 2a, Movie S1).[27-30, 34-36] The surrounding metal atom (Sn or In) of the active O facilities the adsorption by affording site to the oxygen of HCHO molecule; the additional valence electron of Sn, when compared to In, enables Sn-O (HCHO) more energetically favorable (Figure S6−7). For oxidation, another active O, the closest to the dioxymethylene, captures the H atom, generating one formate and one rooted hydroxyl group

(OH_{rooted}), with E_a of 0.68 eV (Figure 3a). The whole reaction energy (E_{react}) reaches −3.72 eV. Mulliken charge analysis (Table 2) reveals that sufficient charge transfer (0.440 *e*) takes place only after the generation of the formate and the OH_{rooted} (Eq. 3b). The C loses more electrons, suggesting being oxidized. The OH_{rooted} (actually it's *H) also makes some contribution. The oxidation process weakens the interaction among the active O and surface metal ions (Figure 3a, right panel 1 and 2), explaining the decrease of νInO and νSnO around 1000 cm^{-1} in HCHO atmosphere.

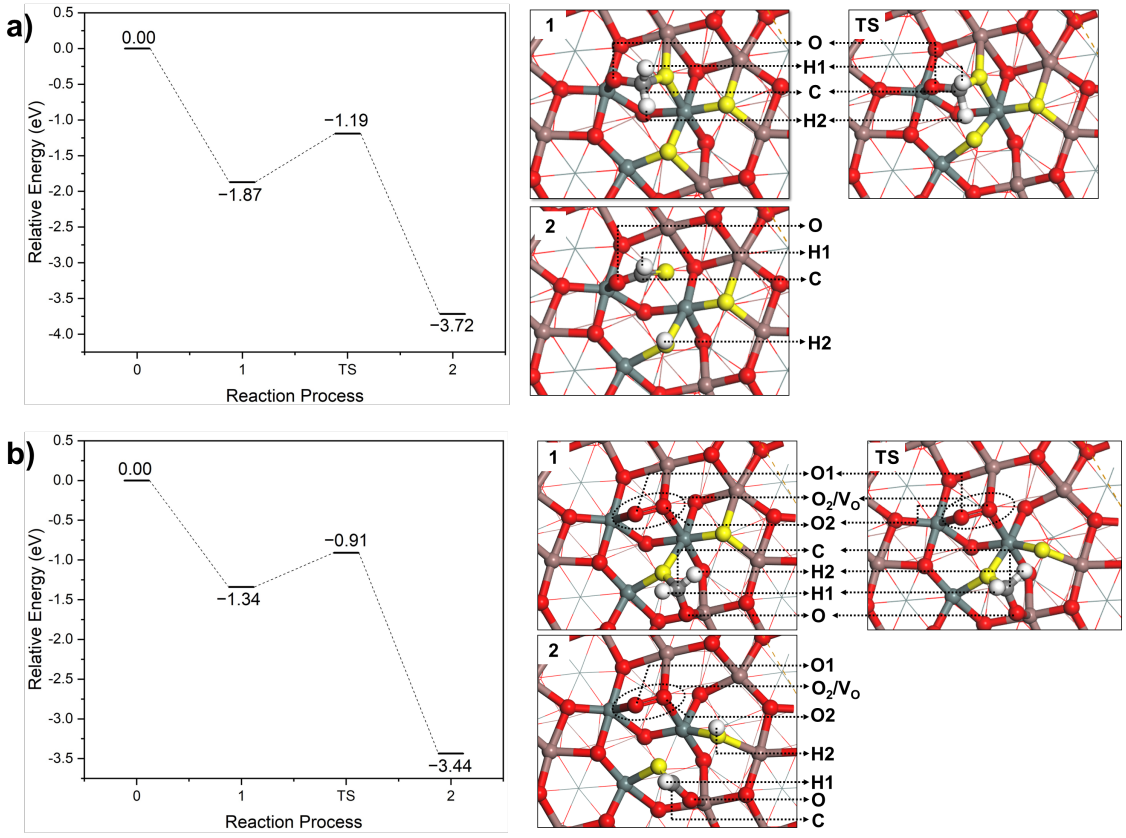

Figure 3 HCHO adsorption and oxidation at: (a) Stoichiometric $In_4Sn_3O_{12}$ (001) and (b) $In_4Sn_3O_{12}$ (001)_O_2/V_O (H, C, O, In, Sn; the bright yellow atom is the active O; TS means transition state.)

Table 2 Mulliken charge analysis of absorbed species at $In_4Sn_3O_{12}$ (001)

Surface	Process	Mulliken charge / *e*							
		HCHO							
$In_4Sn_3O_{12}$ (001)		Total	H1	H2	C	O			
	1	−0.040	0.101	0.105	0.338	−0.584			
	2	0.440	0.095	0.289	0.469	−0.413			
		HCHO					$O_{2\ ads}$		
$In_4Sn_3O_{12}$ (001)_O_2/V_O		Total	H1	H2	C	O	Total	O1	O2
	0						−0.733	−0.337	−0.396
	1	−0.053	0.103	0.106	0.325	−0.587	−0.748	−0.343	−0.405
	2	0.476	0.097	0.289	0.491	−0.401	−0.787	−0.367	−0.420
		HCHO					OH_t		
$In_4Sn_3O_{12}$ (001)_OH_t		Total	H1	H2	C	O	Total	H	O
	0						−0.341	0.284	−0.625
	1	−0.034	0.097	0.117	0.345	−0.593	−0.268	0.357	−0.625
	2	−0.020	0.113	0.107	0.333	−0.573	−0.289	0.332	−0.621
	3	−0.010	0.120	0.115	0.323	−0.568	−0.233	0.296	−0.529
	4	0.366	0.077	0.299	0.438	−0.448	−0.153	0.296	−0.449

Note: The *e* is the elementary electron charge. Positive value represents electron donation effect of adsorbate. The H1, H2 are labeled in Figure 3−4, and the O1, O2 in Figure 3b.

Gaseous O_2 molecule is revealed by DFT simulation to have little interaction with the stoichiometric $In_4Sn_3O_{12}$ (001) but have a high tendency to fill the V_O (Figure S8−10), the defect which is always present due to the high-temperature synthesis of $In_4Sn_3O_{12}$.[8] Even with O_2/V_O, HCHO still interacts with and then is oxidized by the active O, Sn (3a)-connected, with total E_{react} of −3.34 eV and a little lower E_a of 0.43 eV (Figure 3b, Figure S8), and donates electrons (0.476 *e*) to the surface with a few moving to the O_2/V_O (Table 2). Consequently, the O−O bond is elongated from 1.444 to 1.471 Å. The O_2 molecule can dissociate and fill the two V_O, eventually re-generating a stoichiometric surface (Figure S11), once the product (HCOOH) is desorbed to leave the second V_O. This could explain the experimentally observed decrease of the vibration at 1134 cm^{-1} ($\nu O_{2\ ads}$) (Figure 2b, d, g) and gives credence to the hypothesis that the adsorbed molecular oxygen is a precursor for the regeneration of the active O.[11-13, 16]

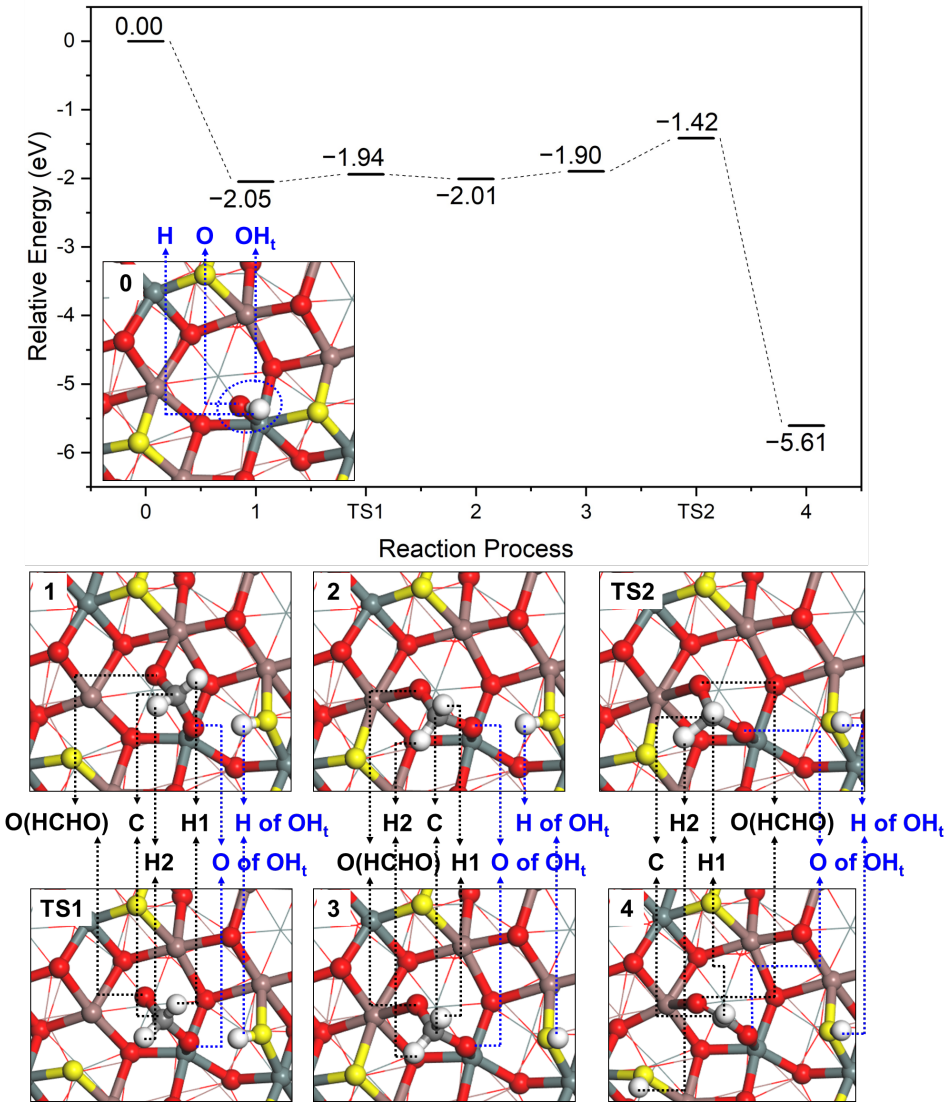

Figure 4 HCHO adsorption and oxidation at $In_4Sn_3O_{12}$ (001)_OH_t

The surface OH_t has already been demonstrated to be able to facilitate the HCHO oxidation.[28-30, 37-38] Numerous OH_t is present at the surface, as demonstrated by the H_2O-D_2O exchange DRIFTS (Figure S5), even in dry air (humidity contamination around 100 ppm) at 200 °C. The HCHO prefers to interact with the OH_t to form the dioxymethylene with E_{ads} −2.05 eV (Figure 3, Movie S2), while the active O accepts the H atom from the OH_t to generate an OH_{rooted}. The migration of the H (D) of the OH_t (OD_t) to the OH_{rooted} (OD_{rooted}) provides an opportunity for the re-generation of OH_t (OD_t) by reaction with O_2 molecules in the recovery stage (Eq. 4); this explains the emergence of νOD_t at 2690 cm^{-1} (Figure 2d).

$$2OH_{rooted}+O_2 \rightarrow 2OH_t+2O_o \qquad \text{Eq. 4a}$$

$$2OD_{rooted}+O_2 \rightarrow 2OD_t+2O_o \quad \text{Eq. 4b}$$

After the adsorption, the dioxymethylene can swing at the triangle (Sn-In-In) and be oxidized when it is close to another active O with E_a of 0.48 eV (Figure 3). The last step makes the most charge contribution (0.366 *e*, Table 2).

3.3 Partial oxidation

The DRIFTS result demonstrates the partial oxidation of HCHO, and the DFT simulation details the reaction route and energy profile as well as the remarkable charge effect of the generated formate and OH_{rooted}. Why in neither the response nor the recovery stage is the formate further oxidized into CO_2 or CO? Some experiments of HCOOH desorption and decomposition demonstrated that on metal oxide surfaces the formate can hardly decompose into CO and CO_2 at 200 °C.[39-40] Some theoretical works have revealed that the energy barrier to break the second C−H bond is much higher than to break the first C−H bond of HCHO.[35, 37] The active O, which is responsible for both HCHO adsorption and HCHO partial oxidation into HCOOH, must also play the key role in further oxidation of HCOOH. The problem is that, under dynamic conditions, the continuously provided HCHO always occupies, by adsorption, and consumes, by partial oxidation, the active O, which has little chance to further oxidize the formate. Especially, under exposure to 10 ppm HCHO, the molecularly adsorbed HCHO present at the surface is demonstrated by the emergence of C=O (HCHO) vibration at 1788 cm^{-1} in Figure 2g. This finding suggests the available active O is not even sufficient to enable the HCHO adsorption as dioxymethylene, letting alone to oxidize the formate. The opetation temperature of 200 °C even weakens the oxidizing ability and slows down the dissociation process. Additionally, the O_2 molecule prefers to be adsorbed at the V_O which is left by the desorbed HCOOH; in this way the O_2 molecule has little chance to be adsorbed nearby and then oxidize the formate.

It is reasonable to consider that if the O_2 content is higher or the HCHO concentration is lower the combustion of HCHO may take place. Taking an extreme example, if the HCHO DRIFTS is measured in pure O_2 background, we believe the HCHO will be completely oxidized into CO_2 and H_2O. However, the sensor signal will not be high, because the surface is easily to be re-oxidized. Actually, we did perform the HCHO DRIFTS at lower concentration of O_2 (20,000 ppm), as shown in Figure S13. Firstly, one can find that the resistance change is larger in the presence of 20,000 ppm O_2 when the sensor is exposed to the same concentration of HCHO. This fact confirms our conclusion that the re-adsorbed molecular oxygen is a

precursor for the regeneration of the active O. The lower O_2 partial pressure definitely slows down the regeneration/re-oxidation of the SMOX surface. Secondly, there is little difference between the DRIFTS results in synthetic air and at 20,000 ppm O_2. The νC=O at 1788 cm^{-1} from molecularly HCHO can also be identified in Figure S13c. This suggests that the oxidation products changes little when the O_2 concentration increases from 20,000 ppm to 205, 000 ppm (synthetic air), which makes it more convincing that the formate is difficult to be further oxidized.

The temperature can also be an important factor for further oxidation of formate specie. With increasing temperature, fewer HCHO molecules are adsorbed, while the density of the active O, as lattice oxygen, should be less influenced. Also, the higher temperature is beneficial for the high-energy-barrier oxidation of formate. It will be interesting to explore the reaction in higher temperature. However, one must notice that, the sensor signal decreases when the temperature exceeds 200 °C (Figure S2).

Finally, this research demonstrates that there is a big gap between the partial oxidation of HCHO into formate specie and the further oxidation of formate. The gap should be taken into consideration when we design HCHO SMOX sensors.

4. Conclusion

The partial oxidation of HCHO into formate (or HCOOH) is responsible for the sensor signal of $In_4Sn_3O_{12}$ under HCHO exposure at 200 °C. The Sn (3a)-connected O is the active site and plays key roles in both HCHO adsorption and partial oxidation. The presence of OH_t facilitates the HCHO adsorption. The partial oxidation can induce sufficient charge transfer. The E_a for the rate-determining-step of the partial oxidation, i.e. the rupture of the first C−H bond of the dioxymethylene, is in medium range (0.43−0.68 eV), making it feasible at the optimum temperature of 200 °C.

Acknowledgements

We acknowledge the valuable inputs from Anna Staerz and the assistance in experiments from Matthias Boepple, Benjamin Junker and Andre Sackmann. For the computational resources, we are grateful for the support from the Research Centre for Materials Genome Engineering at Wuhan University of Technology, the Shenzhen HUASUAN Technology Company Limited and CALMIP (Grant P16038).

Supporting Information Available

Energies of all the configurations, some material characterization, temperature-dependent sensor signal to HCHO, N_2-O_2 DRIFTS, H_2O-D_2O exchange DRIFTS, HCHO DRIFTS in 20,000 ppm background, and some DFT supporting figures. This material is available free of charge via the internet at http://pubs.acs.org.

References

1. Yu, C.; Crump, D., A Review of the Emission of VOCs from Polymeric Materials Used in Buildings. *Build. Environ.* **1998**, *33*, 357-374.

2. Jones, A. P., Indoor Air Quality and Health. *Atmos. Environ.* **1999**, *33*, 4535-4564.

3. Collins, J. J.; Ness, R.; Tyl, R. W.; Krivanek, N.; Esmen, N. A.; Hall, T. A., A Review of Adverse Pregnancy Outcomes and Formaldehyde Exposure in Human and Animal Studies. *Regul. Toxicol. Pharmacol.* **2001**, *34*, 17-34.

4. Izawa, K.; Ulmer, H.; Staerz, A.; Weimar, U.; Barsan, N., 5 - Application of SMOX-Based Sensors. In *Gas Sensors Based on Conducting Metal Oxides*, Barsan, N.; Schierbaum, K., Eds. Elsevier: 2019; pp 217-257.

5. Barsan, N.; Schierbaum, K., *Gas Sensors Based on Conducting Metal Oxides*; Elsevier, 2018.

6. Barsan, N.; Koziej, D.; Weimar, U., Metal Oxide-Based Gas Sensor Research: How To? *Sens. Actuators, B* **2007**, *121*, 18-35.

7. Yamazoe, N., Toward Innovations of Gas Sensor Technology. *Sens. Actuators, B* **2005**, *108*, 2-14.

8. Kemmler, J. A.; Pokhrel, S.; Birkenstock, J.; Schowalter, M.; Rosenauer, A.; Bârsan, N.; Weimar, U.; Mädler, L., Quenched, Nanocrystalline $In_4Sn_3O_{12}$ High Temperature Phase for Gas Sensing Applications. *Sens. Actuators, B* **2012**, *161*, 740-747.

9. Kemmler, J., $In_4Sn_3O_{12}$-Metastable Semiconducting Metal Oxide for Gas Sensing Applications. Ph.D. Dissertation, University of Tübingen, 2015.

10. Staerz, A.; Weimar, U.; Barsan, N., Current State of Knowledge on the Metal Oxide Based Gas Sensing Mechanism. *Sens. Actuators, B* **2022**, *358*, 131531.

11. Gurlo, A., Interplay between O_2 and SnO_2: Oxygen Ionosorption and Spectroscopic Evidence for Adsorbed Oxygen. *ChemPhysChem* **2006**, *7*, 2041-2052.

12. Yuan, H., et al., ZnO Nanosheets Abundant in Oxygen Vacancies Derived from Metal-Organic Frameworks for ppb-Level Gas Sensing. *Adv. Mater.* **2019**, *31*, 1807161.

13. Kim, K.; Choi, P. g.; Itoh, T.; Masuda, Y., Catalyst-Free Highly Sensitive SnO_2 Nanosheet Gas Sensors for Parts Per Billion-Level Detection of Acetone. *ACS Appl. Mater. Interfaces* **2020**, *12*, 51637-51644.

14. Yang, T.; Liu, Y.; Jin, W.; Han, Y.; Yang, S.; Chen, W., Investigation on the Transformation of Absorbed Oxygen at ZnO $\{10\bar{1}0\}$ Surface Based on a Novel Thermal Pulse Method and Density Functional Theory Simulation. *ACS Sens.* **2017**, *2*, 1051-1059.

15. Yang, T.; Jin, W.; Liu, Y.; Li, H.; Yang, S.; Chen, W., Surface Reactions of CH_3OH, NH_3 and CO on ZnO Nanorod Arrays Film: DFT Investigation for Gas Sensing Selectivity Mechanism. *Appl. Surf. Sci.* **2018**, *457*, 975-980.

16. Hübner, M.; Simion, C. E.; Haensch, A.; Barsan, N.; Weimar, U., CO Sensing Mechanism with WO_3 Based Gas Sensors. *Sens. Actuators, B* **2010**, *151*, 103-106.

17. Chu, X.; Chen, T.; Zhang, W.; Zheng, B.; Shui, H., Investigation on Formaldehyde Gas Sensor with ZnO Thick Film Prepared through Microwave Heating Method. *Sens. Actuators, B* **2009**, *142*, 49-54.

18. Park, H. J.; Choi, N.-J.; Kang, H.; Jung, M. Y.; Park, J. W.; Park, K. H.; Lee, D.-S., A ppb-Level Formaldehyde Gas Sensor Based on CuO Nanocubes Prepared Using a Polyol Process. *Sens. Actuators, B* **2014**, *203*, 282-288.

19. Li, Y.; Chen, N.; Deng, D.; Xing, X.; Xiao, X.; Wang, Y., Formaldehyde Detection: SnO_2 Microspheres for Formaldehyde Gas Sensor with High Sensitivity, Fast Response/Recovery and Good Selectivity. *Sens. Actuators, B* **2017**, *238*, 264-273.

20. Xu, R.; Zhang, L.-X.; Li, M.-W.; Yin, Y.-Y.; Yin, J.; Zhu, M.-Y.; Chen, J.-J.; Wang, Y.; Bie, L.-J., Ultrathin SnO_2 Nanosheets with Dominant High-Energy {001} Facets for Low Temperature Formaldehyde Gas Sensor. *Sens. Actuators, B* **2019**, *289*, 186-194.

21. Wicker, S.; Guiltat, M.; Weimar, U.; Hémeryck, A.; Barsan, N., Ambient Humidity Influence on CO Detection with SnO_2 Gas Sensing Materials. A Combined DRIFTS/DFT Investigation. *J. Phys. Chem. C* **2017**, *121*, 25064-25073.

22. Delley, B., From Molecules to Solids with the Dmol3 Approach. *J. Phys. Chem.* **2000**, *113*, 7756-7764.

23. Delley, B., An All‐Electron Numerical Method for Solving the Local Density Functional for Polyatomic Molecules. *J. Phys. Chem. C* **1990**, *92*, 508-517.

24. Delley, B., Hardness Conserving Semilocal Pseudopotentials. *Phys. Rev. B* **2002**, *66*, 155125.

25. Nadaud, N.; Lequeux, N.; Nanot, M.; Jové, J.; Roisnel, T., Structural Studies of Tin-Doped Indium Oxide (ITO) and $In_4Sn_3O_{12}$. *J. Solid State Chem.* **1998**, *135*, 140-148.

26. O'Neil, D. H.; Walsh, A.; Jacobs, R. M. J.; Kuznetsov, V. L.; Egdell, R. G.; Edwards, P. P., Experimental and Density-Functional Study of the Electronic Structure of $In_4Sn_3O_{12}$. *Phys. Rev. B* **2010**, *81*, 085110.

27. Davydov A A, Sheppard N T. Molecular spectroscopy of oxide catalyst surfaces. Chichester: Wiley, 2003.

28. Zhang, C.; Liu, F.; Zhai, Y.; Ariga, H.; Yi, N.; Liu, Y.; Asakura, K.; Flytzani-Stephanopoulos, M.; He, H., Alkali-Metal-Promoted Pt/TiO_2 Opens a More Efficient Pathway to Formaldehyde Oxidation at Ambient Temperatures. *Angew. Chem., Int. Ed.* **2012**, *51*, 9628-9632.

29. Li, Y.; Chen, X.; Wang, C.; Zhang, C.; He, H., Sodium Enhances Ir/TiO_2 Activity for Catalytic Oxidation of Formaldehyde at Ambient Temperature. *ACS Catal.* **2018**, *8*, 11377-11385.

30. Chen, X.; He, G.; Li, Y.; Chen, M.; Qin, X.; Zhang, C.; He, H., Identification of a Facile Pathway for Dioxymethylene Conversion to Formate Catalyzed by Surface Hydroxyl on TiO_2-Based Catalyst. *ACS Catal.* **2020**, *10*, 9706-9715.

31. Degler, D.; Junker, B.; Allmendinger, F.; Weimar, U.; Barsan, N., Investigations on the Temperature-Dependent Interaction of Water Vapor with Tin Dioxide and Its Implications on Gas Sensing. *ACS Sens.* **2020**, *5*, 3207-3216.

32. Schilling, C.; Ganduglia-Pirovano, M. V.; Hess, C., Experimental and Theoretical Study on the Nature of Adsorbed Oxygen Species on Shaped Ceria Nanoparticles. *J. Phys. Chem. Lett.* **2018**, *9*, 6593-6598.

33. Boehme, I.; Weimar, U.; Barsan, N., Unraveling the Surface Chemistry of CO Sensing with In_2O_3 Based Gas Sensors. *Sens. Actuators, B* **2021**, *326*, 129004.

34. Zhou, J.; Mullins, D. R., Adsorption and Reaction of Formaldehyde on Thin-Film Cerium Oxide. *Surf. Sci.* **2006**, *600*, 1540-1546.

35. Teng, B.-T.; Jiang, S.-Y.; Yang, Z.-X.; Luo, M.-F.; Lan, Y.-Z., A Density Functional Theory Study of Formaldehyde Adsorption and Oxidation on CeO_2 (111) Surface. *Surf. Sci.* **2010**, *604*, 68-78.

36. Busca, G.; Lamotte, J.; Lavalley, J. C.; Lorenzelli, V., FT-IR Study of the Adsorption and Transformation of Formaldehyde on Oxide Surfaces. *J. Am. Chem. Soc.* **1987**, *109*, 5197-5202.

37. Wang, X.; Rui, Z.; Ji, H., DFT Study of Formaldehyde Oxidation on Silver Cluster by Active Oxygen and Hydroxyl Groups: Mechanism Comparison and Synergistic Effect. *Catal. Today* **2020**, *347*, 124-133.

38. Bai, B.; Li, J., Positive Effects of K+ Ions on Three-Dimensional Mesoporous Ag/Co_3O_4 Catalyst for HCHO Oxidation. *ACS Catal.* **2014**, *4*, 2753-2762.

39. Durand, J. P.; Senanayake, S. D.; Suib, S. L.; Mullins, D. R., Reaction of Formic Acid over Amorphous Manganese Oxide Catalytic Systems: An in Situ Study. *J. Phys. Chem. C* **2010**, *114*, 20000-20006.

40. Fein, D. E.; Wachs, I. E., Quantitative Determination of the Catalytic Activity of Bulk Metal Oxides for Formic Acid Oxidation. *J. Catal.* **2002**, *210*, 241-254.

TOC graphic

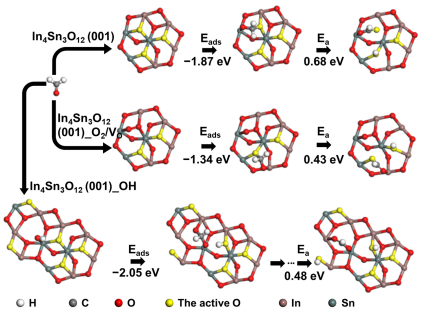
In4Sn3O12 (001)
Eads
−1.87 eV
Ea
0.68 eV
In4Sn3O12 (001)_O2/VO
Eads
−1.34 eV
Ea
0.43 eV
In4Sn3O12 (001)_OH
Eads
−2.05 eV
Ea
0.48 eV
H
C
O
The active O
In
Sn

Supporting Information

HCHO Sensing Mechanism of $In_4Sn_3O_{12}$ Revealed by DRIFTS and DFT

Tingqiang Yang,[1,2] Anne Hemeryck,[2,*] Suman Pokhrel,[3] Wen Chen,[4] Lutz Mädler,[3] Udo Weimar,[1] Nicolae Barsan[1,*]

[1] Institute of Physical and Theoretical Chemistry and Center for Light-Matter Interaction, Sensors & Analytics (LISA+), University of Tübingen, 72076 Tübingen, Germany

[2] LAAS-CNRS, Université de Toulouse, CNRS, 31400 Toulouse, France

[3] Foundation Institute of Materials Science (IWT), Department of Production Engineering, University of Bremen, 28359 Bremen, Germany

[4] State Key Laboratory of Silicate Materials for Architectures, School of Materials Science and Engineering, Wuhan University of Technology, 430070 Wuhan, China

***Corresponding authors:**

Nicolae Barsan: nb@ipc.uni-tuebingen.de

Anne Hemeryck: anne.hemeryck@laas.fr

Table S1 Total energies of all the configurations

Configuration		Total energy in Hatree
Molecules	O_2	−150.2457730
	HCHO	−114.4162309
The optimized $In_4Sn_3O_{12}$ primitive cell		−5075.3072174
The optimized $In_4Sn_3O_{12}$ (001) super surface cell		−27068.6689985
$In_4Sn_3O_{12}$ (001)_HCHO	Figure S7a	−27183.1540494
	Figure S7b	−27183.1338576
	Figure S7c	−27183.1137639
	Figure S7d	−27183.1107369
	Figure S7e	−27183.1414466
	Figure S7f	−27183.1337517
	Figure 3a Panel 1	−27183.1540494
	Figure 3a Panel TS	−27183.1290808
	Figure 3a Panel 2	−27183.2218184
$In_4Sn_3O_{12}$ (001)_V_O	Figure S8a	−26993.4877714
	Figure S8b	−26993.4964254
	Figure S8c	−26993.4837929
	Figure S8d	−26993.4748411
	Figure S8e	−26993.4788766
	Figure S8f	−26993.4710771
$In_4Sn_3O_{12}$ (001)_O_2	Figure S9a,b	−27218.8973715
	Figure S9c,d	−27218.8992612
	Figure S9e,f	−27218.9030621
$In_4Sn_3O_{12}$ (001)_ O_2/V_O	Figure S10a	−27143.7842705
	Figure S10b	−27143.7906369
	Figure S10c	−27143.7463335
	Figure S10d	−27143.7398000
$In_4Sn_3O_{12}$ (001)_O_2/V_O_HCHO	Figure S11a	−27258.2467621
	Figure S11b	−27258.2218561
	Figure S11c	−27258.2233867
	Figure S11d	−27258.2274897
	Figure S11e	−27258.2381089
	Figure S11f	−27258.2561840
	Figure S11g	−27258.2358608
	Figure S11h	−27258.2386216
	Figure 3b Panel 1	−27258.2561840
	Figure 3b Panel TS	−27258.2403535
	Figure 3b Panel 2	−27258.3331799
$In_4Sn_3O_{12}$ (001)_OH		−27144.4236986

$In_4Sn_3O_{12}$ (001)_OH_HCHO	Figure 4b Panel 1	−27258.9152075
	Figure 4b Panel TS1	−27258.9113168
	Figure 4b Panel 2	−27258.9137587
	Figure 4b Panel 3	−27258.9096315
	Figure 4b Panel TS2	−27258.8919994
	Figure 4b Panel 4	−27259.0460075

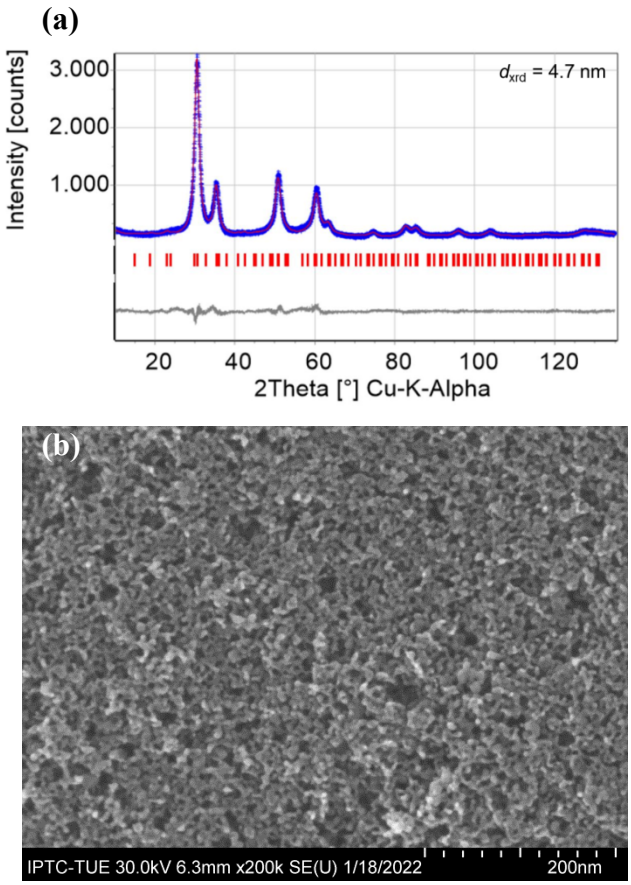

Figure S1 (a) XRD Rietveld refinement and (b) SEM image of $In_4Sn_3O_{12}$

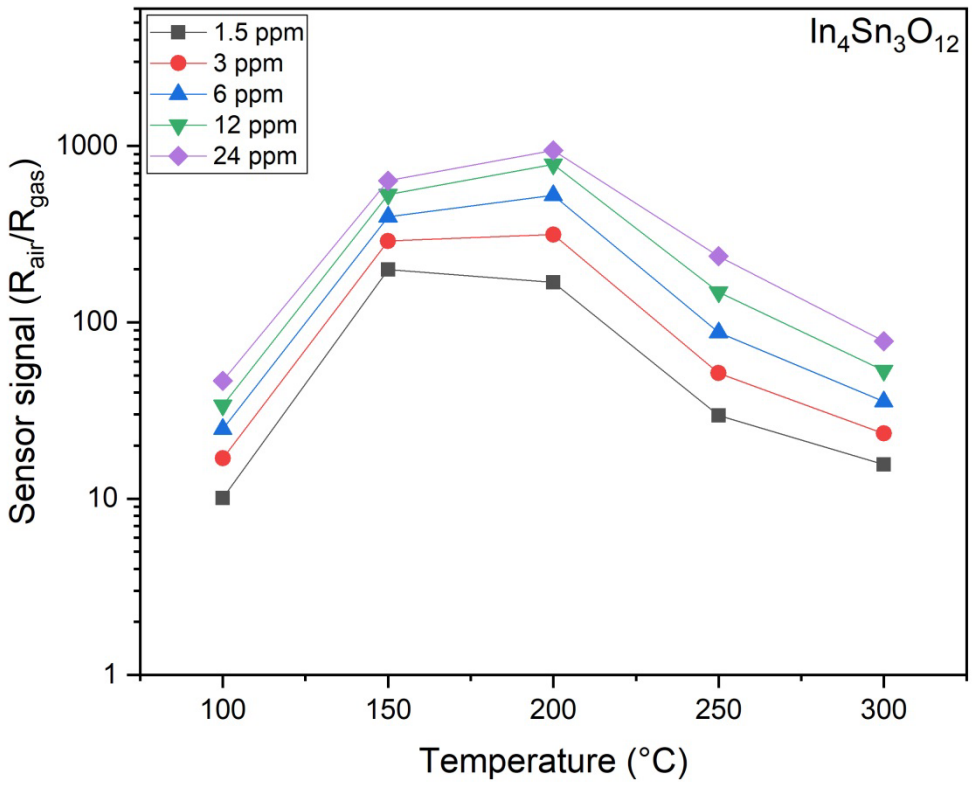

Figure S2 Sensor signal of $In_4Sn_3O_{12}$ to HCHO at different temperature at 50 % relative humidity

The differences between the sensor signals reported previously and the ones reported here are due to the different method used for the deposition of the sensing layer; previously, the sensing layer deposition was performed directly in the FSP reactor, which resulted in extremely porous layers; because of that the sensor signals were larger but the DRIFTS signals were lower – they depend on the number of interactions/scattering taking place in the sensing layer, which scales with the sensing layer density. Because the sensing layer realized by the screen printing of inks based on FSP synthesized powders is denser than that the directly FSP-deposited one, the sensor signal is lower but the DRIFTS one is larger.[1] Additionally, the HCHO is measured at higher concentration to compare with the HCHO DRIFTS measurement in which high concentration is necessary to make infrared signal more evident.

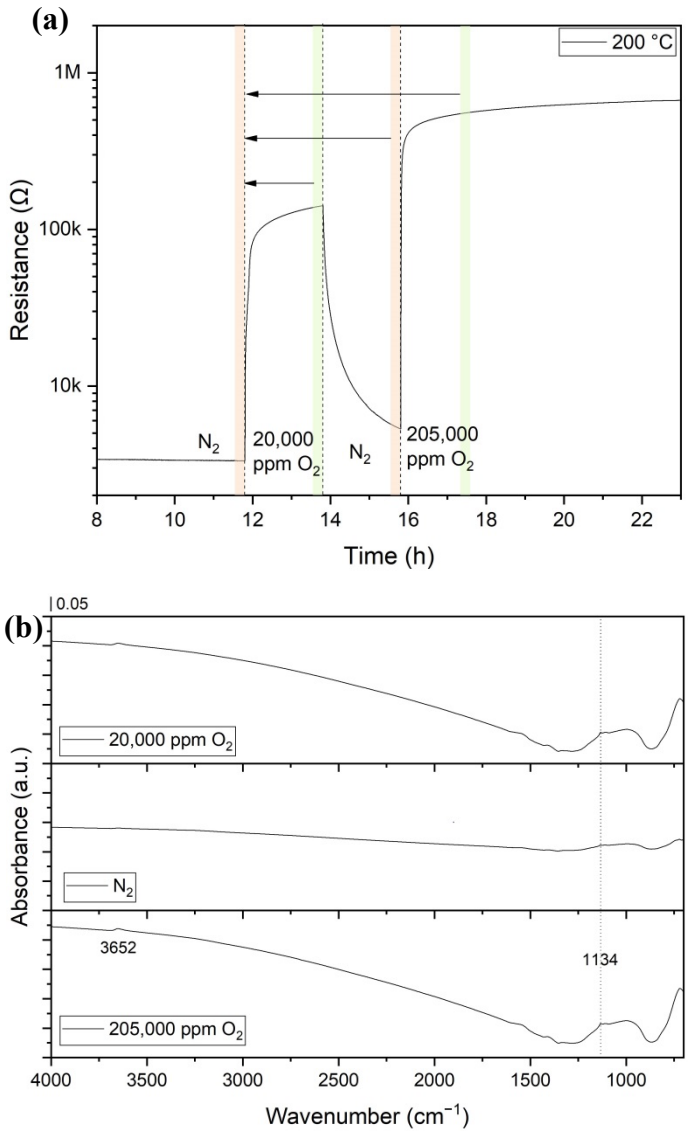

Figure S3 N_2-O_2 DRIFTS: (a) Resistance curve and (b) absorbance spectra referred to the initial single channel spectrum in N_2 (There is still around 20 ppm O_2 in even N_2)

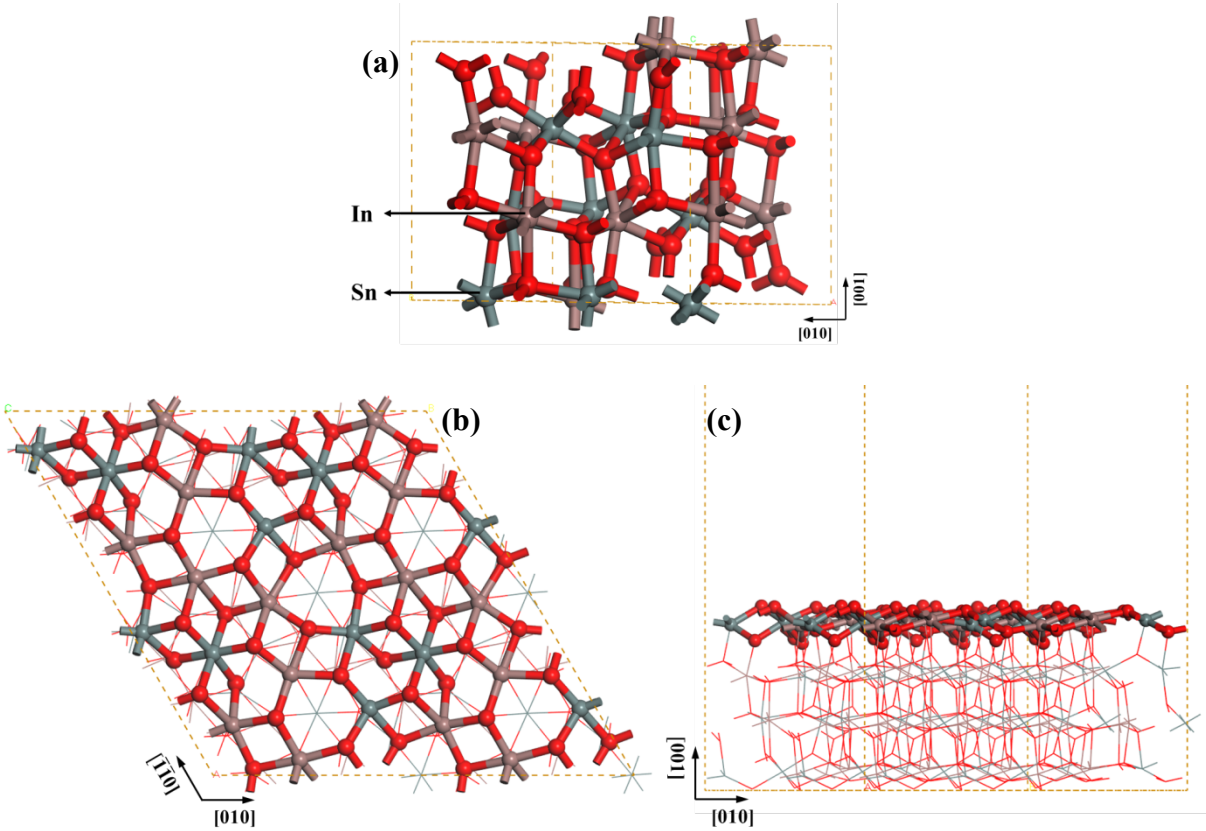

Figure S4 (a) The optimized $In_4Sn_3O_{12}$ primitive cell, and (b, c) the optimized (2 × 2) supercell of $In_4Sn_3O_{12}$ (001) surface (The upmost layer is displayed in ball and stick, while others in line.)

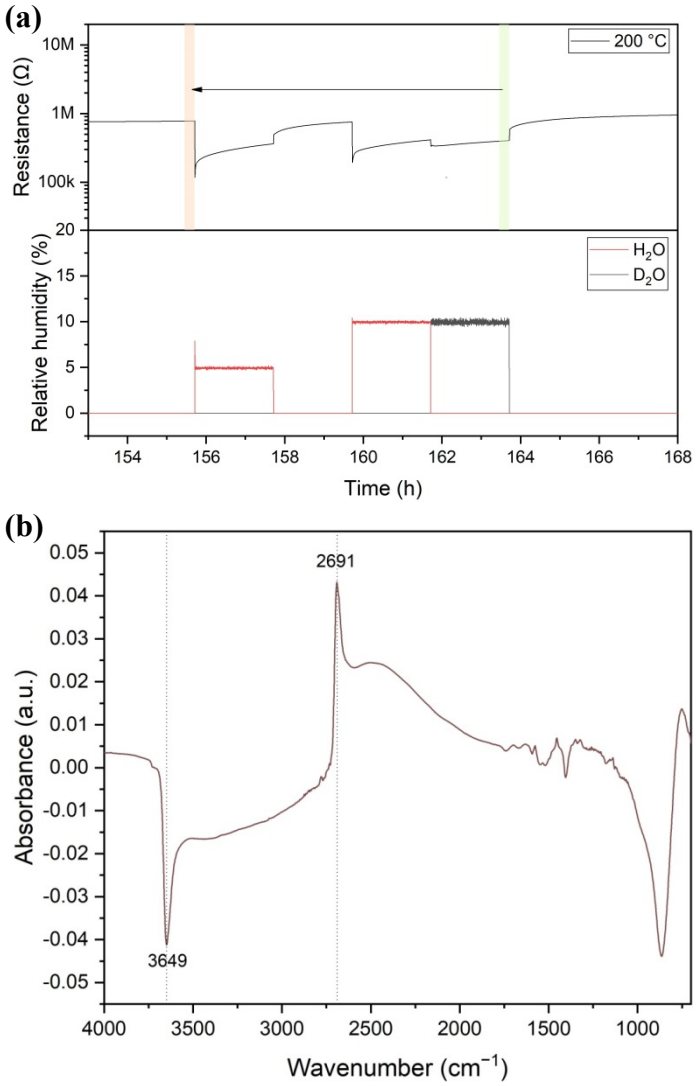

Figure S5 H_2O-D_2O exchange DRIFTS at 200 °C: (a) Resistance curve and (b) absorbance spectrum by referring the SC spectrum in 10 % r.h. D_2O to that in dry synthetic air

The sharp decrease and peak at 3649 cm^{-1} and 2691 cm^{-1} induced by D_2O exchange demonstrates the vibration at 3649 cm^{-1} and 2691 cm^{-1} should be attributed to terminal OH (OH_t) and terminal OD (OD_t), respectively.[2] Additionally, because the reference is the single channel (SC) spectrum in dry synthetic air, the sharp decrease at 3649 cm^{-1} suggests there are many terminal hydroxyl groups even in dry synthetic air at 200 °C.

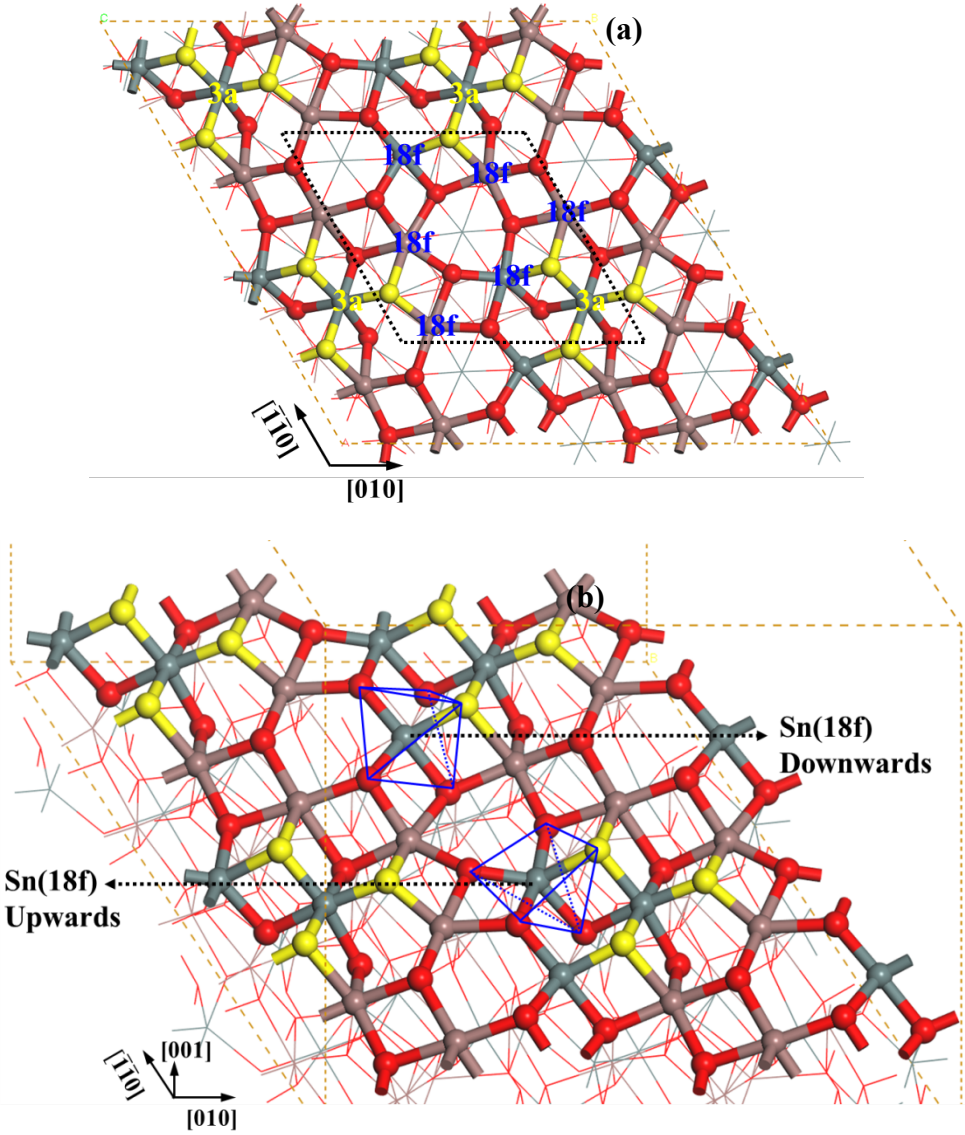

Figure S6 Optimized (2 × 2) supercell of $In_4Sn_3O_{12}$ (001) surface

The bright yellow is the oxygen atom connected with Sn (3a) at surface. Because of the periodicity, it is sufficient to consider HCHO adsorption in the black frame.

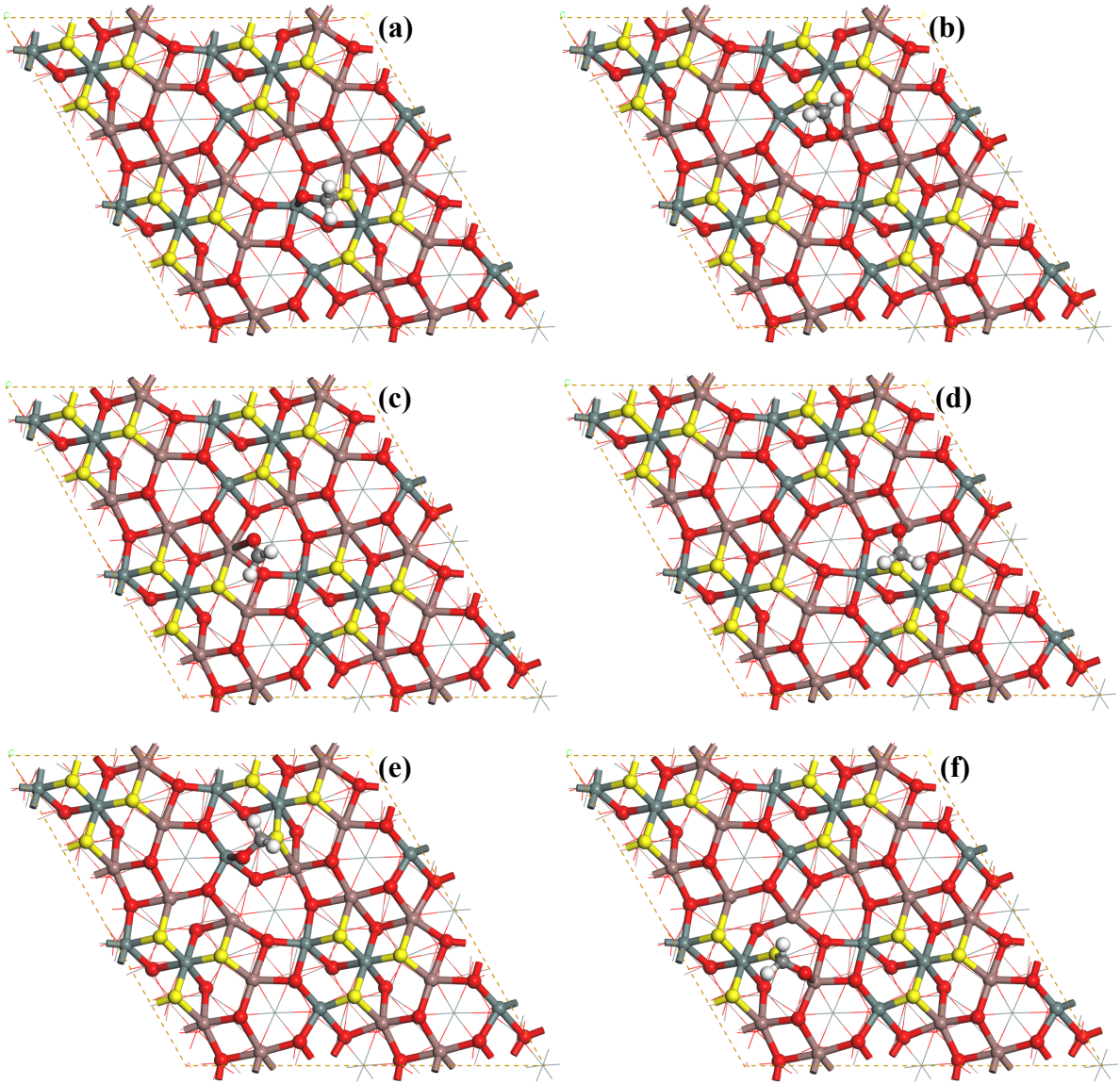

Figure S7 HCHO adsorption at stoichiometric $In_4Sn_3O_{12}$ (001) in different configuration (The white is H atom and the grey is C atom)

It shows that the O atom of HCHO tends to interact with surface non-fully coordinated 18f metal atom, and the H or C interacts with the Sn (3a)-connected oxygen. The adsorption energy is −1.87 eV, −1.32 eV, −0.78 eV, −0.69 eV, −1.53 eV and −1.32 eV for configuration Figure S7 a ~ f. Thus, it is more energetically favorable to make the O of HCHO interact with Sn (18f), i.e. Figure S7 a, e.

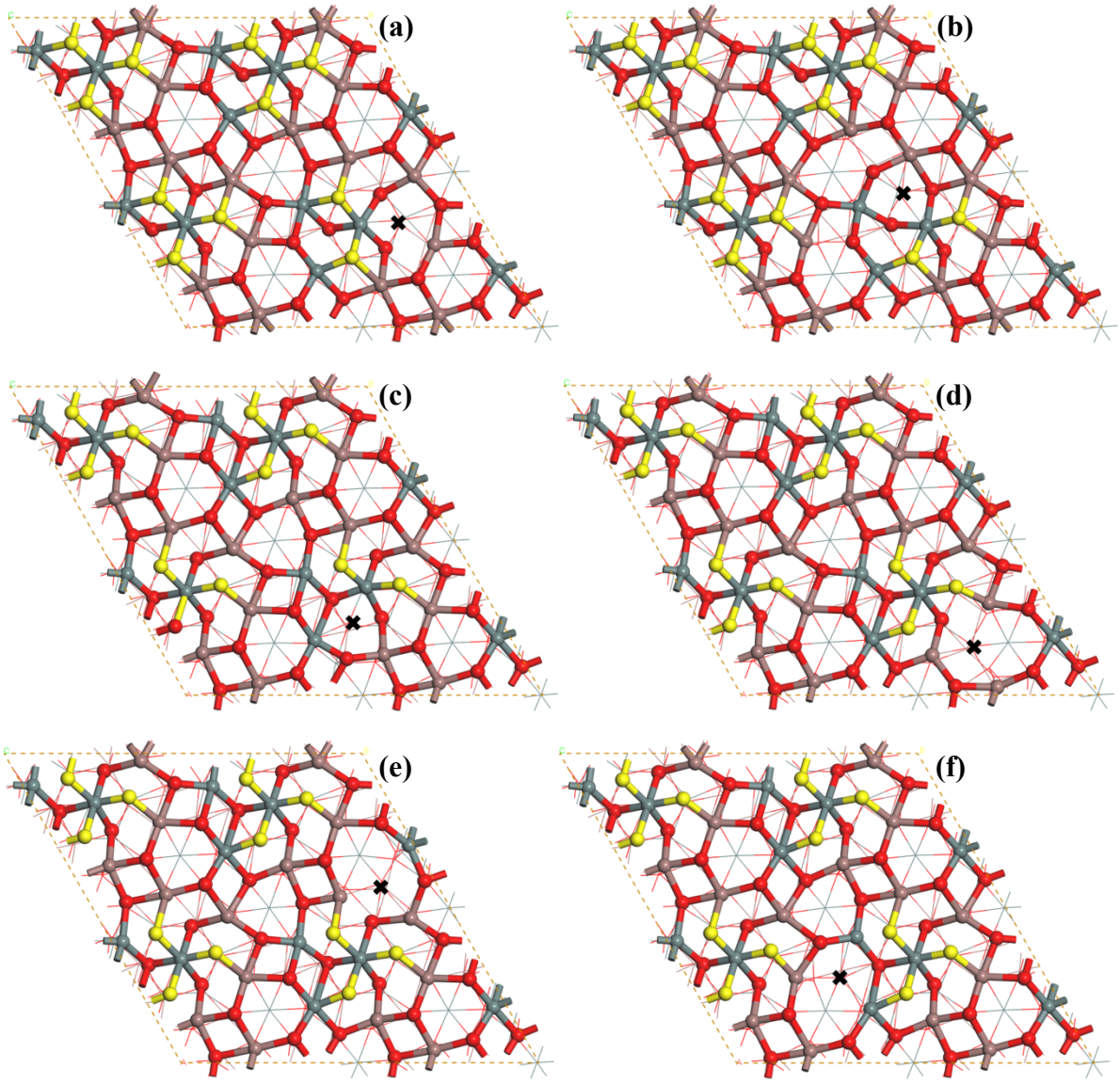

Figure S8 Several possible configurations of oxygen vacancy symbolled by ✖ at $In_4Sn_3O_{12}$ (001)

The formation energy of V_O is 1.59 eV, 1.35 eV, 1.70 eV, 1.94 eV, 1.83 eV and 2.04 eV for configuration Figure S8a ~ f. Thus, the configuration of Figure S8b is more possible.

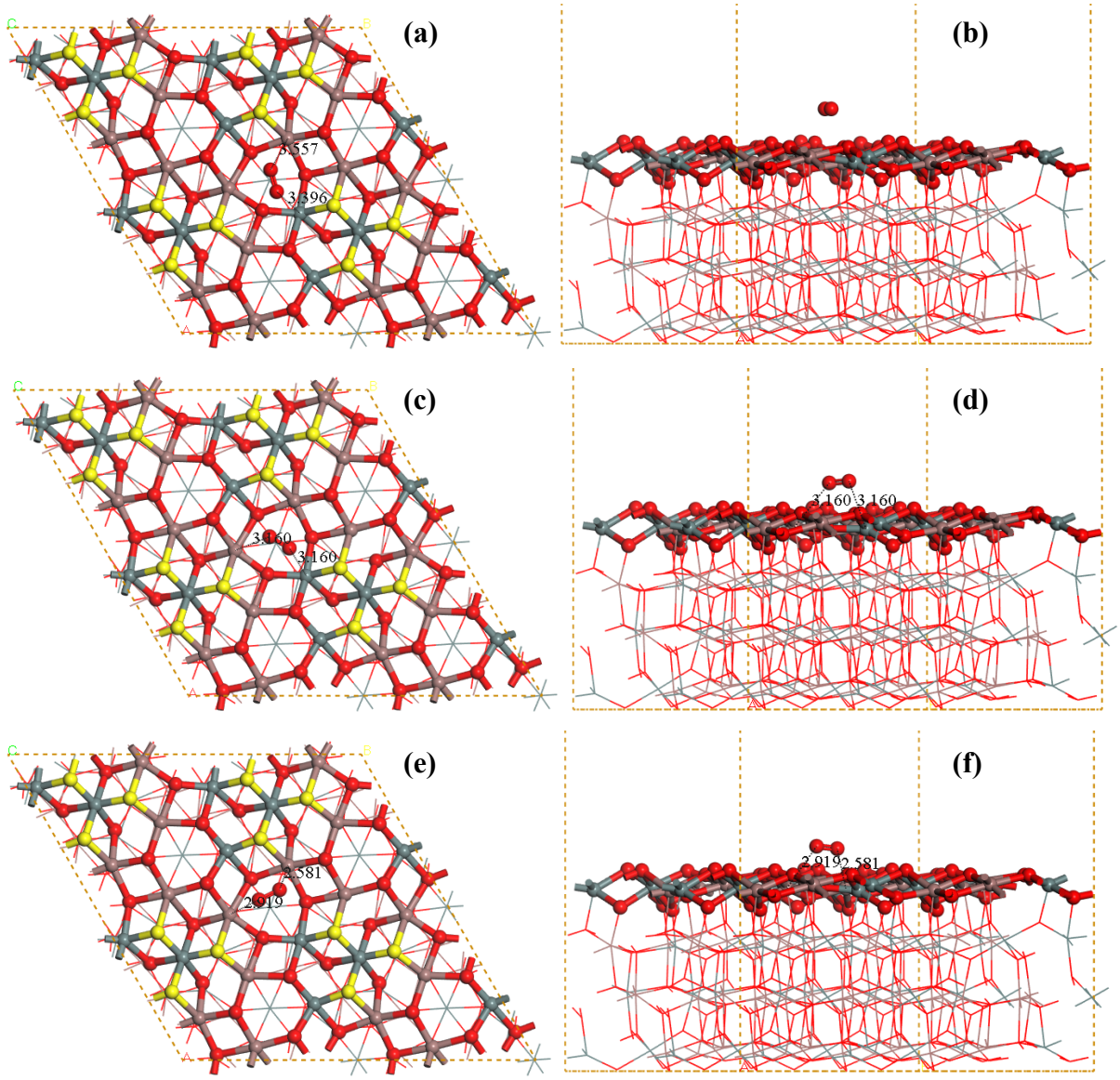

Figure S9 Several possible configurations of O_2 molecule adsorbed at stoichiometric $In_4Sn_3O_{12}$ (001): (a, c, and e) Top views and (b, d, f) front views (The number in black is the distance with unit of Å).

The E_{ads} for O_2 molecule is even positive (0.47 eV for Figure S9a, b; 0.42 eV for Figure S9c, d; 0.32 eV for Figure S9e, f) and no bond is formed, demonstrating little feasibility for adsorption of O_2 molecule at stoichiometric $In_4Sn_3O_{12}$ (001). The positive E_{ads} for O_2 molecule is probably because GGA is known to overstabilize the O_2 molecule.[3]

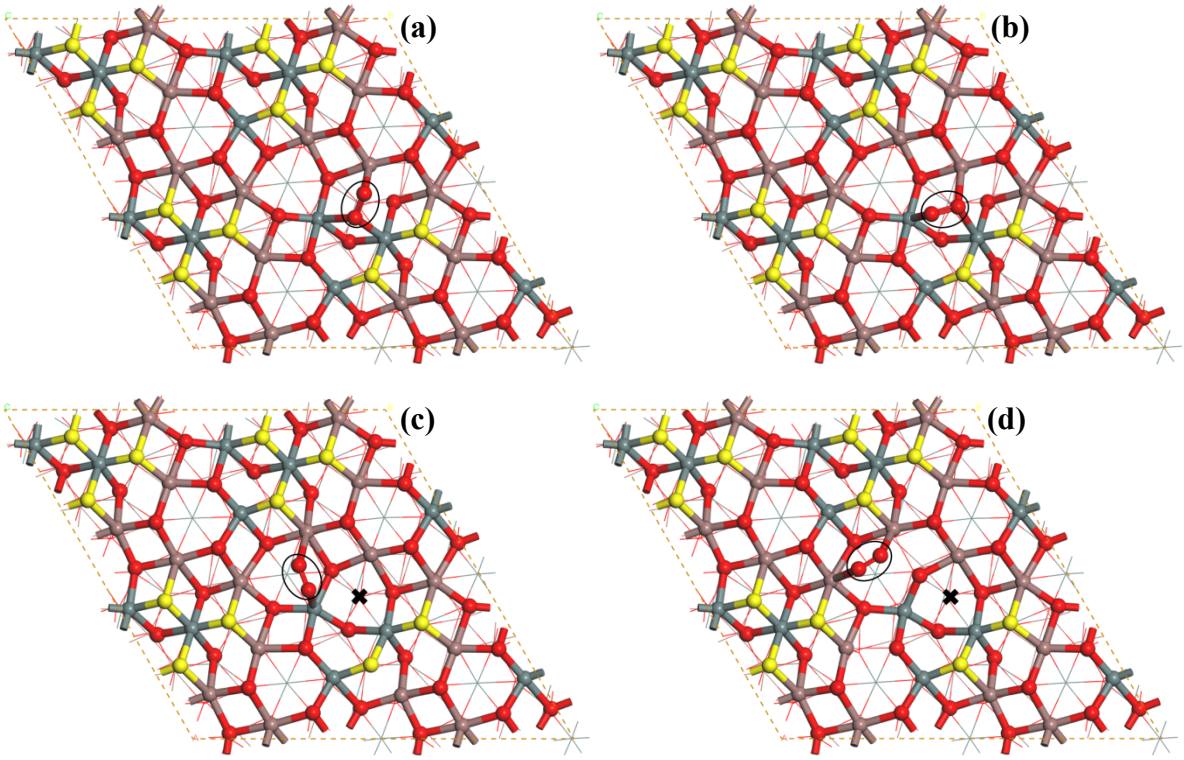

Figure S10 Several possible configurations of O_2 molecule (in black circle) adsorbed at or around V_O at $In_4Sn_3O_{12}$ (001)

The O_2 adsorption energy of V_O is −1.14 eV, −1.32 eV, −0.11 eV and −0.07 eV for configuration Figure S10 a−d. Thus, it is more energetically favorable for O_2 molecule to be adsorbed at V_O like Figure S10 b.

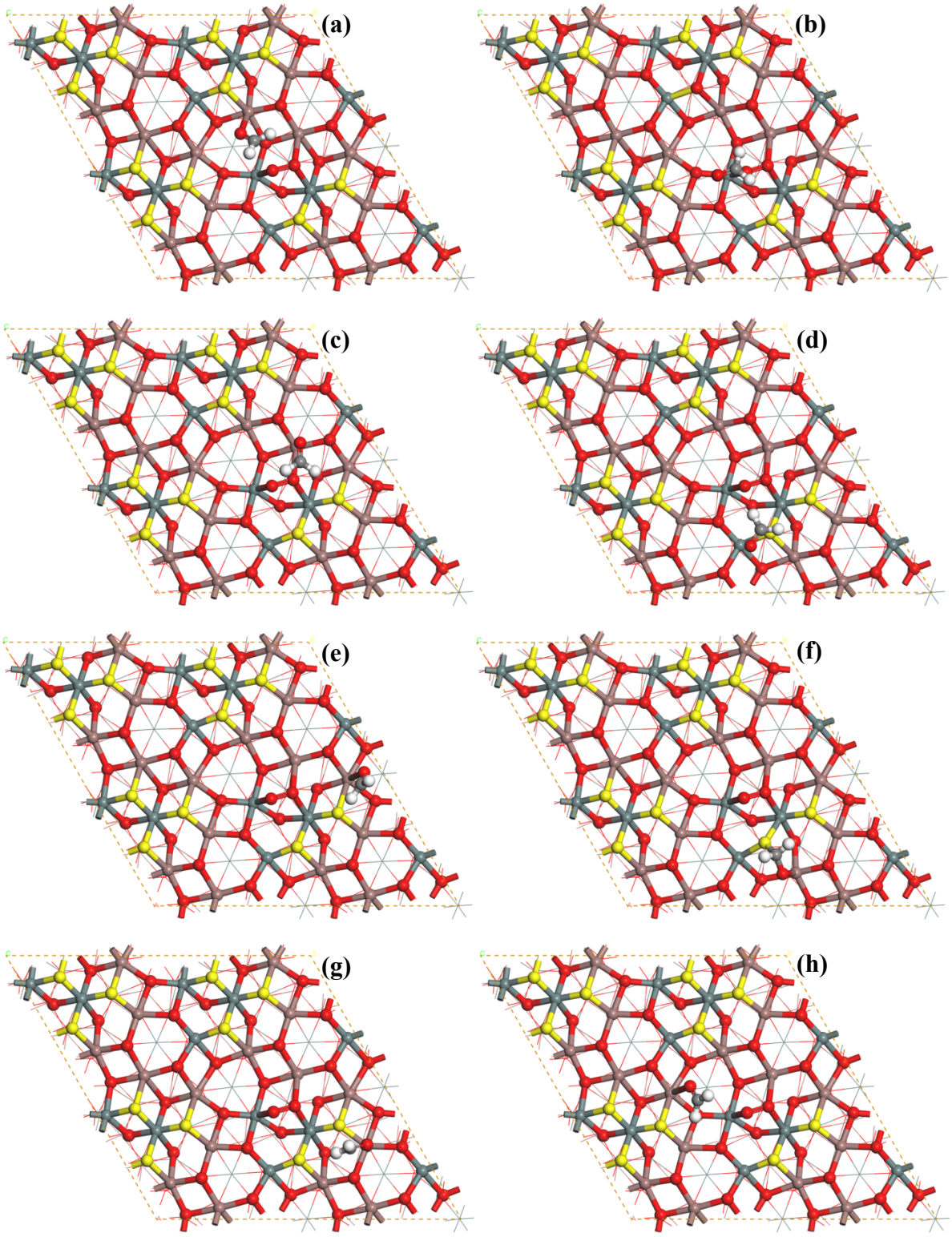

Figure S11 Several possible configurations of HCHO adsorbed at $In_4Sn_3O_{12}$ (001) with O_2/V_O

The HCHO adsorption energy is −1.09 eV, −0.41 eV, −0.45 eV, −0.56 eV, −0.85 eV, −1.34 eV, −0.79 eV and −0.86 eV for configuration Figure S11 a−h. In this (2 × 2) supercell, as can be seen, near the O_2/V_O is some active sites same as the stoichiometric surface for HCHO adsorption. Herein, the attention is paid to the

sites at or around O_2/V_O. According to the results, HCHO still has high tendency to be adsorbed around O_2/V_O. The most energetically favorable adsorption configuration is shown in Figure S11 f, and it is similar to stoichiometric surface (Figure S7 b), the O of HCHO bonding to surface In, and the C to the active O.

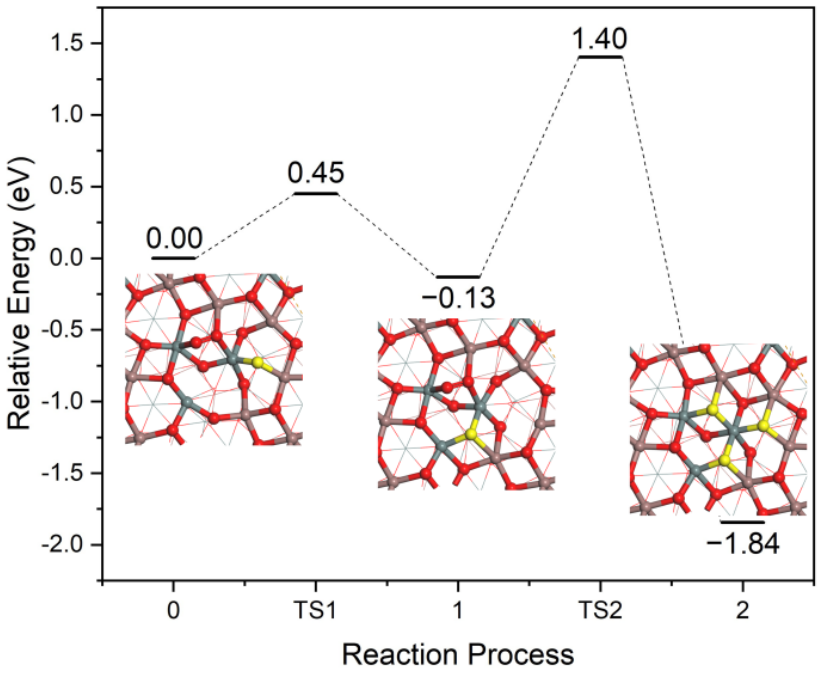

Figure S12 Re-construction of $In_4Sn_3O_{12}$ (001) surface when another V_O is left after desorption of HCOOH in Figure 3b.

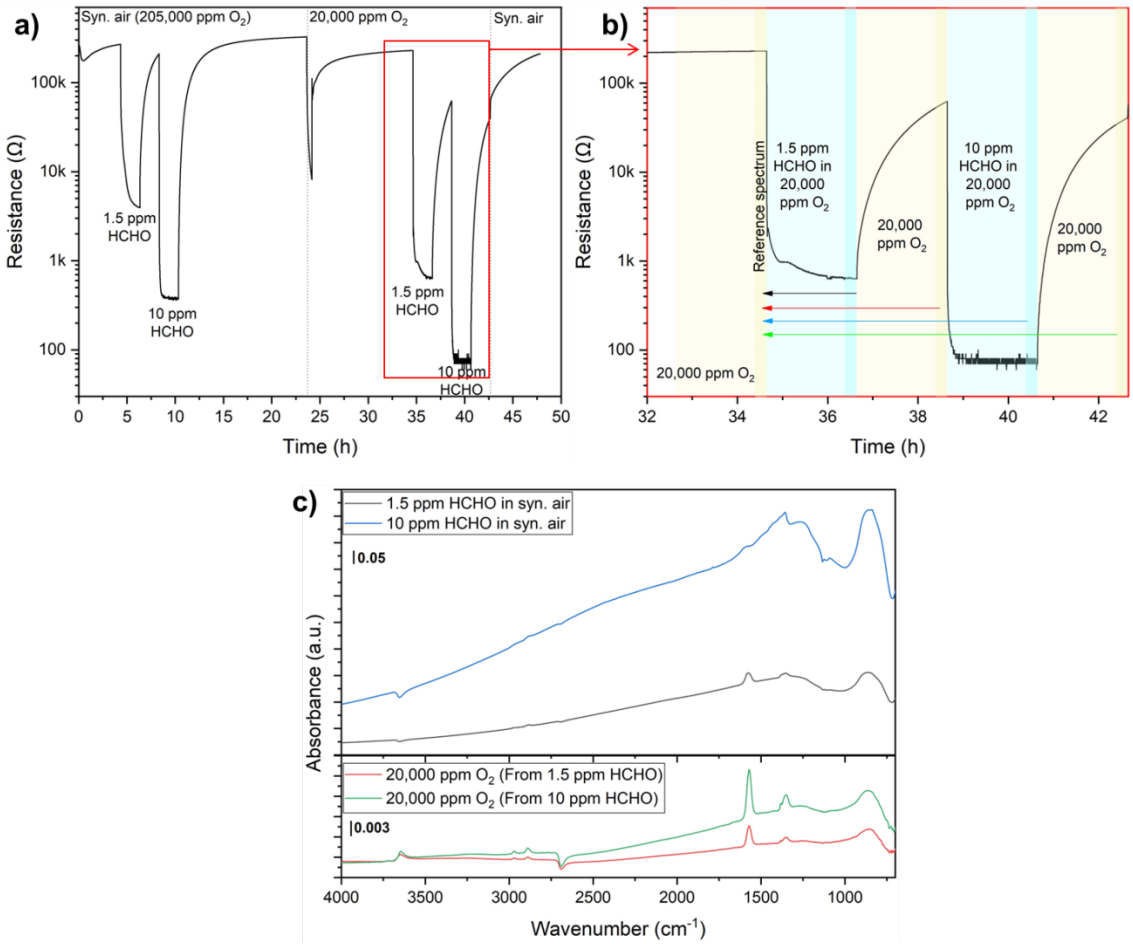

Figure S13 DRIFTS results measured at 200 °C in 20,000 ppm O_2. (a) Resistance curve of the sensor device during HCHO DRIFTS measurement in synthetic air and then in 20,000 ppm O_2, (b) Resistance curve of the sensor device during HCHO DRIFTS in 20,000 ppm O_2, (c) absorbance spectra by referencing the last SC spectra under the 1.5 ppm HCHO exposure, the second air exposure, the 10 ppm HCHO exposure and the third air exposure to the last SC spectrum under first air exposure, as shown in panel b.

References

(1) Kemmler, J. A.; Pokhrel, S.; Birkenstock, J.; Schowalter, M.; Rosenauer, A.; Bârsan, N.; Weimar, U.; Mädler, L. Quenched, nanocrystalline In4Sn3O12 high temperature phase for gas sensing applications. *Sensors and Actuators B: Chemical* **2012**, *161* (1), 740-747. DOI: https://doi.org/10.1016/j.snb.2011.11.026.

(2) Davydov, A. Molecular Spectroscopy of Oxide Catalyst Surfaces. **2003**. Zhang, C.; Liu, F.; Zhai, Y.; Ariga, H.; Yi, N.; Liu, Y.; Asakura, K.; Flytzani-Stephanopoulos, M.; He, H. Alkali-Metal-Promoted Pt/TiO2 Opens a More Efficient Pathway to Formaldehyde Oxidation at Ambient Temperatures. *Angewandte Chemie International Edition* **2012**, *51* (38), 9628-9632. DOI: https://doi.org/10.1002/anie.201202034. Boehme, I.; Weimar, U.; Barsan, N. Unraveling the Surface Chemistry of CO Sensing with In2O3 Based Gas Sensors. *Sensors and Actuators B: Chemical* **2021**, *326*, 129004. DOI: https://doi.org/10.1016/j.snb.2020.129004. Degler, D.; Junker, B.; Allmendinger, F.; Weimar, U.; Barsan, N. Investigations on the Temperature-Dependent Interaction of Water Vapor with Tin Dioxide and Its Implications on Gas Sensing. *ACS Sensors* **2020**, *5* (10), 3207-3216. DOI: 10.1021/acssensors.0c01493. Wicker, S.; Guiltat, M.; Weimar, U.; Hémeryck, A.; Barsan, N. Ambient Humidity Influence on CO Detection with SnO2 Gas Sensing Materials. A Combined DRIFTS/DFT Investigation. *The Journal of Physical Chemistry C* **2017**, *121* (45), 25064-25073. DOI: 10.1021/acs.jpcc.7b06253.

(3) Curtiss, L. A.; Raghavachari, K.; Redfern, P. C.; Pople, J. A. Assessment of Gaussian-2 and density functional theories for the computation of enthalpies of formation. *The Journal of Chemical Physics* **1997**, *106* (3), 1063-1079. DOI: 10.1063/1.473182.